8-15-2005

Multiscale Modeling, Simulations, and Experiments of Coating Growth on Nanofibers. Part Ii. Deposition

A. Buldum

C. B. Clemons

L. H. Dill

K. L. Kreider

G. W. Young

See next page for additional authors

Authors
A. Buldum, C. B. Clemons, L. H. Dill, K. L. Kreider, G. W. Young, X. Zheng, Edward A. Evans, G. Zhang, and S. I. Hariharan

Multiscale modeling, simulations, and experiments of coating growth on nanofibers. Part II. Deposition

A. Buldum
Department of Physics, University of Akron, Akron, Ohio 44325-4001

C. B. Clemons, L. H. Dill, K. L. Kreider, G. W. Young,[a] and X. Zheng
Division of Applied Mathematics, Department of Theoretical and Applied Mathematics, University of Akron, Akron, Ohio 44325-4002

E. A. Evans and G. Zhang
Department of Chemical Engineering, University of Akron, Akron, Ohio 44325-3906

S. I. Hariharan
Department of Electrical and Computer Engineering, University of Akron, Akron, Ohio 44325-3904

(Received 4 January 2005; accepted 30 June 2005; published online 17 August 2005)

This work is Part II of an integrated experimental/modeling investigation of a procedure to coat nanofibers and core-clad nanostructures with thin-film materials using plasma-enhanced physical vapor deposition. In the experimental effort, electrospun polymer nanofibers are coated with aluminum materials under different operating conditions to observe changes in the coating morphology. This procedure begins with the sputtering of the coating material from a target. Part I [J. Appl. Phys. 98, 044303 (2005)] focused on the sputtering aspect and transport of the sputtered material through the reactor. That reactor level model determines the concentration field of the coating material. This field serves as input into the present species transport and deposition model for the region surrounding an individual nanofiber. The interrelationships among processing factors for the transport and deposition are investigated here from a detailed modeling approach that includes the salient physical and chemical phenomena. Solution strategies that couple continuum and atomistic models are used. At the continuum scale, transport dynamics near the nanofiber are described. At the atomic level, molecular dynamics (MD) simulations are used to study the deposition and sputtering mechanisms at the coating surface. Ion kinetic energies and fluxes are passed from the continuum sheath model to the MD simulations. These simulations calculate sputtering and sticking probabilities that in turn are used to calculate parameters for the continuum transport model. The continuum transport model leads to the definition of an evolution equation for the coating-free surface. This equation is solved using boundary perturbation and level set methods to determine the coating morphology as a function of operating conditions. © *2005 American Institute of Physics*. [DOI: 10.1063/1.2007849]

I. INTRODUCTION

This paper is a continuation of Ref. 1, which presented a coordinated experimental and modeling program for the synthesis of core/clad and hollow nanowire structures. Physical vapor deposition techniques were used to apply coatings to electrospun polymer nanofibers. These fibers were coated with films of copper, aluminum, titanium, zirconium, and aluminum nitride by using a plasma-enhanced physical vapor deposition (PEPVD) sputtering process, as shown in Fig. 1.

For reference, some details of the reactor and the synthesized nanowires are described. In the reactor, a power supply drives a 2-in. diameter electrode which forms the target (or source) material. A mat of nanofibers is placed on a holder that sits 8 cm above the target. When a negative electrical potential is applied to the electrode (target), a plasma of positively charged ions forms in the gas phase. The resulting electric field causes these ions to impact the target. These collisions, in turn, sputter neutral species of the target material into the gas phase. Once in the gas phase, the neutral species are transported throughout the reactor and are deposited on all available surfaces, including the nanofibers. Ions from the plasma also strike the coated nanofibers, but typically with much less energy because the substrate is not biased. These collisions tend to smooth out the coating through a re-sputtering process. The coating growth rate depends on the rate at which atoms are supplied to the nanofiber surface, the nanofiber temperature, and the ion flux to the nanofiber. The morphology of the coating depends on the mobility of the atoms on the surface and how much time the atoms have to move around before the next atoms hit the surface. The rate at which atoms are supplied to a nanofiber depends on the rate at which atoms are sputtered from the target. The sputtering rate depends on the ion flux, which is determined by the power applied to the target, the pressure of the system, and the working gas used.

Transmission electron microscopy (TEM) is used to determine the effects of these variables on the film growth rate and morphology. The average thicknesses of the fibers before and after the coating process are compared to determine the

[a]Electronic mail: gwyoung@uakron.edu

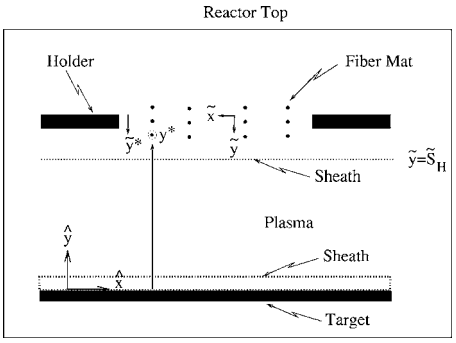

FIG. 1. Global schematic of the reactor for neutral species transport within the reactor.

average growth rate of the coating. To determine the coating morphology and crystalline structure, TEM images and diffraction patterns are taken.

Figure 2 shows a nanofiber coated with aluminum. Following deposition, the polymer nanofiber may be removed by pyrolisis while leaving the coating. Figure 3 shows the open cylindrical cross section of a nanotube created in this fashion. The inner diameter of the tube was around 20 nm in this case. The approximate thickness of the tube walls was controlled by the sputtering process. A tube with 40-nm wall thickness is shown in Fig. 4.

The approach described above can be used to produce cylindrical, multilayered nanostructures with precisely controlled interfaces composed of many materials including metals, semiconductors, ceramics, and polymers with controlled diameters and a range of nanometer-thick walls. In this work the deposition is taking place on nanoscale size structures.[2]

II. OVERALL MODELING APPROACH

To aid in the understanding of the deposition process, a comprehensive model for the coating of nanofibers within a traditional PEPVD system was described in Ref. 1. The objective of the model is to determine the influence of process conditions on the uniformity and morphology of the coating. The system is characterized by a bulk gas phase dominated by neutral species and sheath regions that separate the bulk gas phase from the substrate (nanofibers) and the target, as shown in Fig. 1. There are several disparate geometrical length scales in the reactor system. The reactor size from the target to the top is no more than 20 cm in length. The distance from the target to the holder is centimeters in length. Sheath regions are several millimeters in thickness, while nanofibers range from 20 to 100 nm in diameter. In our modeling effort, we treat each nanofiber within the mat as an isolated fiber, and also assume that the holder region of the nanofibers does not influence the global transport of neutral

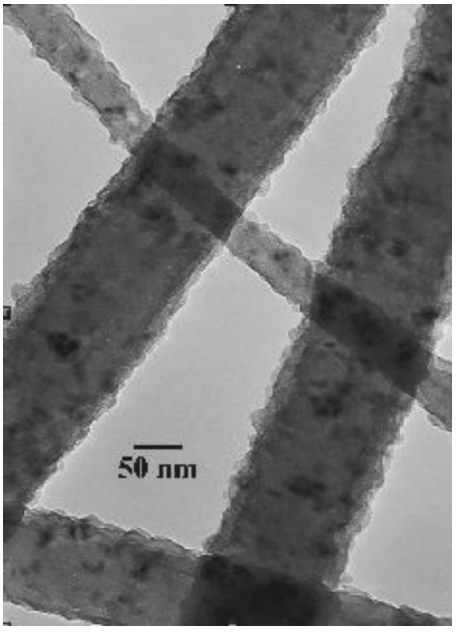

FIG. 2. TEM images of aluminum-coated fibers.

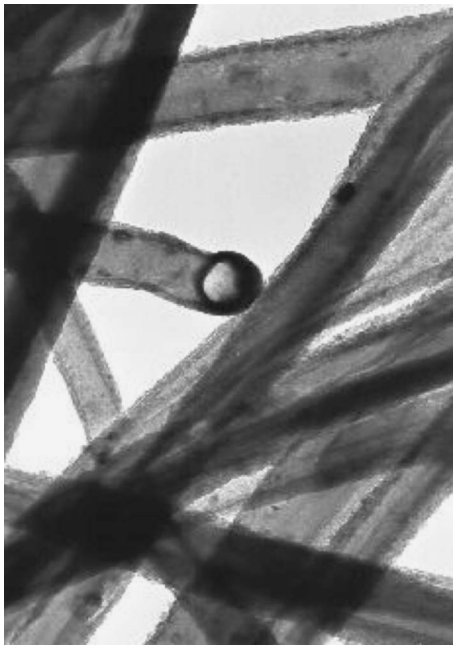

FIG. 3. TEM image of an aluminum nanotube.

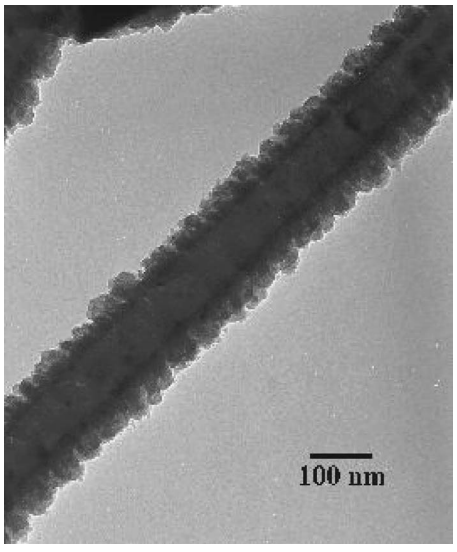

FIG. 4. Aluminum nanotube with a wall thickness of 40 nm.

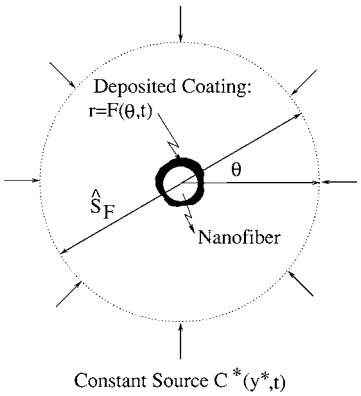

FIG. 5. Local model for neutral species transport near the nanofiber.

species. As noted above, however, a sheath region that influences ion transport does exist in the region of the holder and its mat of nanofibers.

The transport of neutral species is separated into two components: (1) a one-dimensional reactor-scale model and (2) a two-dimensional local nanofiber-scale model. The reactor-scale model, the focus of Ref. 1, includes the sheath region near the target and transport throughout the reactor, but ignores the presence of the holder region. The present paper focuses upon the transport of neutral species in the vicinity of a typical nanofiber. With these assumptions, the two papers are linked as follows: the reactor-scale model provides the far-field (half the distance away from an adjacent fiber) input of the neutral species concentration C^* at location $\hat{y}=y^*$ of a particular nanofiber, as shown in Fig. 1. Figure 5 provides a schematic of the region near a nanofiber. The cylindrical fiber is encapsulated by a nonuniform coating of neutral species. Outside the coating we suppose a sheath region exists and that the far-field neutral species concentration is C^*. We note that the reactor-scale model[1] predicts that this concentration is constant throughout the reactor, except, of course, in the vicinity of the fiber, which is the topic of the present paper.

As noted previously, ions strike the coated fibers with less energy than they do the target. These collisions tend to redistribute the neutral species on the fiber through a resputtering process that is heavily dependent upon the local topography. It follows that the coating process is sensitive to the full range of length scales, from the reactor scale to the fiber scale and the still smaller molecular (or atomistic) scale. Reactor level process variables influence the surface-scale features of the coating. Simultaneously, coating processes at the surface scale can affect the reactor-scale characteristics. Simulation of this feedback between the surface features and the reactor-scale level is difficult to accomplish given the current computational abilities. Thus, efficient solution methodologies integrating simulations at the various length scales must be developed.[3–6] This paper and Ref. 1 present a strategy for accomplishing some portions of this integration through the linking of models at the global reactor scale, the local nanofiber scale, and the molecular scale.

For the remainder of this paper, we consider the nanofiber region and transport of the deposition material by diffusion. Poisson and ion fluid equations govern the transport of ions through the sheath region around the holder, and the interaction of the ions with the coating surface. Mass balance equations at the coating surface include deposition rate parameters and desorption parameters due to ion bombardment. These parameters are functions of the fiber and coating curvature, the ion flux to the coating surface, and the ion kinetic energy. These parameters are passed to the continuum equations from molecular-dynamics (MD) simulations.

At the local nanofiber scale, a polar coordinate geometry is considered in this investigation, and plans to extend this to an axisymmetric configuration are underway. Level set and evolution equation approaches are used to simulate the coating shape. Four basic components of the coating mechanism are included in these approaches. These are attachment kinetics, curvature effects, etching due to ion bombardment, and solid-state diffusion on the coating surface. These equations are solved numerically and analyzed via boundary perturbation techniques. Results from these analyses are shown to verify basic experimental observations, for example, the wavelength and magnitude of the coating roughness is larger in both the axial and azimuthal directions for larger-diameter fibers.

At the atomic level, MD simulations[7] are used to study the adsorption, reflection and sputtering mechanisms, and migration of atoms on the coating. The ion kinetic energy, ion flux, and the thickness of the coating from the continuum models are used as input to the MD simulations. This information serves as the initial condition for the ion bombardment.

Because of the size of the fiber and the computational limitations of the MD approach, it is not possible to simulate the entire circumference of the coating surface. Hence, an angular sector of the nanofiber is examined at fixed coating thicknesses to develop a global picture of the coating growth.

Information concerning the angle of incidence of bombardment on the sector is curve fit to form expressions for the deposition and desorption parameters that are valid around the circumference of the fiber, and which are then passed to the continuum model. The information obtained from the MD simulations at each coating thickness is curve fit to obtain expressions that are continuous in time, for use by the continuum models. This creates a solution methodology that iterates between atomic and continuum models.

Putting all of the above pieces together, level set simulations of the coating front are presented. The initial polymer nanofiber landscape is taken to be a superposition of Fourier modes, consistent with models of the electrospinning process.[8,9] Hence, our approach links models across the entire fabrication process. Predictions of the coating thickness based upon the simulations are compared with our experimental observations. The model we have developed provides reasonable trends with respect to the coating evolution on nanoscale structures and how that evolution depends on process parameters. The next step is to benchmark the model against experimental data as the processing parameters are varied. This benchmarking is the subject of Part III of this series.

III. NEUTRAL SPECIES TRANSPORT MODEL

A. Formulation

In Ref. 1 the dimensional concentration C^* of the neutral species at the reactor scale was found to be the constant,

$$C^* = \frac{k_{\text{ions}}}{k}, \tag{1}$$

where k is a reaction coefficient for sputtered material readsorbing to the target surface and k_{ions} is the desorption rate coefficient for sputtering due to ion bombardment of the target surface. These rate coefficients depend on $\hat{J}^+$, the ion flux to the surface, and $\hat{\epsilon}^+$, the ion kinetic energy. These two quantities were obtained by examining the sheath region around the target. Once determined, these quantities were passed to the MD simulations to determine k and k_{ions}. Knowing these parameters, the concentration C^* was then determined in the reactor as a function of the reactor operating conditions. This concentration field serves as the input for the local transport model as shown in Fig. 5. The main thrust of the present work is to use a coupled continuum/atomistic approach to describe the transport of depositing species local to the vicinity of the nanofiber. Given the sparsity of the nanofiber mesh, it is assumed that the concentration C^* away from a nanofiber is unaffected by any loss of depositing species due to deposition. However, the concentration near the nanofiber does change due to the deposition. Note also that the units of concentration are mole/volume, the units of k are length/time, and the units of k_{ions} are mole/(area $\times$ time).

For the local nanofiber-scale transport model around a single nanofiber, we consider a cylindrical geometry as shown in Fig. 5. This particular nanofiber is located at a distance $\hat{y}=y^*$ from the target as shown in Fig. 1. The goal is to determine the location, $\hat{r}=\hat{F}(\theta,\hat{t})$, of the front of the deposited coating. We assume that the source of the deposition material is given by C^*, and is located at $\hat{r}=\hat{S}_F$, where $\hat{S}_F$ is half the average spacing between fibers in the mat. This value C^* remains constant around the nanofiber because the fiber is so small in comparison to the global reactor scale. Since C^* is a result of the sputtering process and depends on the reactor operating conditions, we have linked the *local* and *global* models through the condition at $\hat{r}=\hat{S}_F$.

Within the local region surrounding a fiber $[\hat{F}(\theta,\hat{t}) \leqslant \hat{r} \leqslant \hat{S}_F]$, we assume that the concentration $\hat{c}$ of the deposition material (neutral gas molecules) is large compared to the ion concentration, and that the mode of transport of the deposition material is primarily governed by diffusion,

$$\frac{\partial \hat{c}}{\partial \hat{t}} = \hat{D}\left[\frac{\partial^2 \hat{c}}{\partial \hat{r}^2} + \frac{1}{\hat{r}}\frac{\partial \hat{c}}{\partial \hat{r}} + \frac{1}{\hat{r}^2}\frac{\partial^2 \hat{c}}{\partial \theta^2}\right], \tag{2}$$

where $\hat{D}$ is the mass diffusion coefficient.

At the coating front $[\hat{r}=\hat{F}(\theta,\hat{t})]$, the diffusive flux of the neutral species equals the net rate of deposition due to (i) deposition (or reaction) from the bulk phase and (ii) desorption due to ion bombardment of the coating surface. These two processes correspond to the respective terms on the right-hand side of

$$\hat{D}\,\nabla\,\hat{c}\cdot\hat{n} = k_F(\theta,\hat{I}_F^+,\hat{\epsilon}_F^+,\hat{F})\hat{c}[1-\hat{\Gamma}\,\hat{\kappa}] - k_{F\text{ions}}(\theta,\hat{I}_F^+,\hat{\epsilon}_F^+,\hat{F}). \tag{3}$$

Equations of this form have previously been proposed in Refs. 10–12. Here k_F is a reaction coefficient, $\hat{\Gamma}$ the capillary length scale, $\hat{\kappa}$ the curvature of the front, $k_{F\text{ions}}$ the desorption rate coefficient due to ion bombardment of the coating surface, $\hat{I}_F^+$ the ion flux to the surface, and $\hat{\epsilon}_F^+$ the ion kinetic energy. The latter two quantities are obtained by examining the sheath region around the holder. This analysis is described in Sec. IV.

The surface reaction-rate coefficents, k_F and $k_{F\text{ions}}$, are dependent upon the flux and energy of the ions as well as the angle of incidence to the coating surface and the thickness of the coating. The MD simulations in Sec. V are used to develop expressions for these coefficients.

The normal velocity of the coating front, $\hat{v}_n$, is needed to simulate the film growth at this length scale, using the level set method. The normal front velocity is taken to be

$$\hat{v}_n = k_F\beta\hat{c}[1-\hat{\Gamma}\,\hat{\kappa}] - \beta k_{F\text{ions}} - \psi_s D_s \hat{\Gamma}\frac{\partial^2 \hat{\kappa}}{\partial \hat{s}^2}, \tag{4}$$

where β is the molar volume, $\hat{s}$ the arclength along the coating front, and ψ_s the thickness of the coating film that participates in the surface diffusion phenomenon. The units for β are determined by $\beta=(\text{mwt})(1/\text{density})=\text{vol/mole}$, where the density is that for the coating in the solid phase and mwt is the molecular weight of the coating material. Equations similar to (4) have been proposed in Refs. 12 and 13 for chemical-vapor deposition onto flat substrates.

All of the terms in (4) are evaluated on the front, $\hat{r}=\hat{F}(\theta,\hat{t})$. The first two terms in this equation are the contributions to the normal velocity due to deposition and desorption, and the third term is diffusion along the coating surface. Here D_s is the diffusivity of the adatoms on the coating surface. The coating surface, in the two-dimensional Euclidean vector space, is given by

$$\hat{\mathbf{r}}(\theta,\hat{t}) = \langle \hat{F}(\theta,\hat{t})\cos\theta, \hat{F}(\theta,\hat{t})\sin\theta\rangle, \tag{5}$$

so that the curvature of the front is

$$\hat{\kappa}(\theta,\hat{t}) = \frac{\hat{F}^2(\theta,\hat{t}) + 2\hat{F}_\theta^2(\theta,\hat{t}) - \hat{F}(\theta,\hat{t})\hat{F}_{\theta\theta}(\theta,\hat{t})}{[\hat{F}_\theta^2(\theta,\hat{t}) + \hat{F}^2(\theta,\hat{t})]^{3/2}}. \tag{6}$$

The normal vector to the coating front is

$$\hat{n} = \frac{\langle \hat{F}_\theta \sin\theta + \hat{F}\cos\theta, -\hat{F}_\theta\cos\theta + \hat{F}\sin\theta\rangle}{\sqrt{\hat{F}_\theta^2 + \hat{F}^2}}. \tag{7}$$

The normal front velocity $\hat{v}_n$ is also defined by

$$\hat{v}_n = \frac{d\hat{\mathbf{r}}}{d\hat{t}}\cdot\hat{n}. \tag{8}$$

Setting (4) equal to (8) allows one to develop an evolution equation for the shape of the coating front. In addition to a level set simulation, this equation is analyzed via the boundary perturbation method. In this case, the front is assumed to have the form

$$|\mathbf{r}| = \hat{F}(\theta,\hat{t}) = \hat{f}(\hat{t}) + \hat{A}\hat{g}(\theta,\hat{t}), \tag{9}$$

where $\hat{A}$ is the amplitude of the angular perturbation to the base state growth front, $\hat{f}(\hat{t})$. We assume that $\hat{A}$ is small and that there are two sources for angular variation in the system. One source is the initial shape of the nanofibers, which are nearly circular in cross section. The other source is the variation of $k_{F\text{ions}}$ and k_F with respect to θ. These parameters depend upon θ due to the electric field that develops in the holder region. This point is elaborated upon in Sec. V. The boundary perturbation analysis complements the level set simulations of more complicated growth shapes.

The governing equations and boundary conditions are nondimensionalized using the following scalings:

Dimensional variable	Scale
$\hat{c}$	C^*
$\hat{r}$	$\hat{S}_F$
$\hat{t}$	$\hat{S}_F/(K_F\beta C^*)$
$\hat{s}$—arclength	$\hat{S}_F$

Here K_F is a constant representing the average value of k_F. Dimensionless variables are hatless. These scalings lead to the nondimensional groups

$$D_{k_F} = (k_F\hat{S}_F)/\hat{D},$$

$$\Gamma = \hat{\Gamma}/\hat{S}_F,$$

$$Q_F = K_F\hat{S}_F\beta C^*/\hat{D} \ll 1,$$

where D_{k_F}, the Damköhler number, is the ratio of the rate of deposition on the fiber to the rate of neutral species transport by diffusion, and Q_F is the ratio of the rate of front motion to the rate of diffusion of the neutral species.

The nondimensional governing equation for concentration is

$$Q_F c_t = c_{rr} + \frac{1}{r}c_r + \frac{1}{r^2}c_{\theta\theta} \quad \text{for } F(\theta,t) < r < 1. \tag{10}$$

Here, $F(\theta,t)=\hat{F}(\theta,\hat{t})/\hat{S}_F$ is the dimensionless coating thickness. We impose two spatial boundary conditions upon the concentration field. At the edge of the local region ($r=1$), the concentration is uniform as predicted by the reactor-scale model,

$$c = 1. \tag{11}$$

At the edge of the coating $[r=F(\theta,t)]$, we apply the dimensionless version of (3):

$$\frac{c_r - (F_\theta/F)^2 c_\theta}{\sqrt{1+(F_\theta/F)^2}} = D_{k_F}c(1-\Gamma\kappa) - \frac{k_{F\text{ions}}\hat{S}_F}{C^*\hat{D}}, \tag{12}$$

where

$$\kappa = \frac{F^2 + 2F_\theta^2 - FF_{\theta\theta}}{[F^2+F_\theta^2]^{3/2}} \tag{13}$$

is the nondimensional curvature.

The coating front velocity (4) in dimensionless form is

$$\frac{\langle F_t\cos\theta, F_t\sin\theta\rangle \cdot \langle (F\sin\theta)_\theta, (-F\cos\theta)_\theta\rangle}{\sqrt{F_\theta^2+F^2}} = \frac{k_F}{K_F}c(1-\Gamma\kappa) - \frac{k_{F\text{ions}}}{K_F C^*} - \frac{\psi_s D_s}{\beta C^* K_F \hat{S}_F^2}\Gamma\frac{\partial^2\kappa}{\partial s^2}. \tag{14}$$

Note that $\partial^2\kappa/\partial s^2 = (\kappa_\theta/\sqrt{F^2+F_\theta^2})_\theta/\sqrt{F^2+F_\theta^2}$ is the second derivative of curvature with respect to arclength, so (14) takes the form

$$\frac{FF_t}{\sqrt{F^2+F_\theta^2}} = \frac{k_F}{K_F}c(1-\Gamma\kappa) - \frac{k_{F\text{ions}}}{K_F C^*} - \frac{\psi_s D_s\Gamma}{\beta C^* K_F \hat{S}_F^2}\frac{(\kappa_\theta/\sqrt{F^2+F_\theta^2})_\theta}{\sqrt{F^2+F_\theta^2}}. \tag{15}$$

This expression is used to develop an evolution equation for the dynamic location of the coating front.

B. Solutions

Based upon our experimental observations, the growth rates of the coatings are very slow while the mass diffusivities are quite large at these pressures. The TEM images of some, but not all, coated nanofibers indicate that the coatings are nearly circular. Given this observation and if the nanofibers are sparse, then the concentration gradient and the rate constants around the nanofibers should be independent of angle as a leading-order approximation.

As a result of these observations, we make three assumptions to make analytical progress in the solution of the above system of equations: (i) the rate of growth of the front compared to the rate of diffusional transport is negligible ($Q_F \ll 1$, so the system is quasistatic), (ii) the coating is nearly circular, and (iii) derivatives of the concentration and of the two rate constants with respect to θ are negligible at leading order.

The Appendix describes a solution to the above equations using the boundary perturbation expansion

$$F(\theta,t) = f(t) + Ag(\theta,t), \quad A \ll 1, \tag{16}$$

where $A=\hat{A}/\hat{S}_F$, and g is a small perturbation (with amplitude $\hat{A}$) of the boundary front from the growing circular front, $r=f(t)$.

To obtain a weakly nonlinear evolution equation to define the shape, $F(\theta,t)$, of the coating front, we use assumptions (i) and (iii) above. In particular we assume that the shape of the coating does not significantly influence the transport of c in the θ direction. The solution procedure for

(10) and boundary conditions (11)–(15) is now similar to that used by the boundary perturbation analysis (in the Appendix), except that the front shape is no longer expanded as in (16) and the etching terms are retained. We find that

$$c = 1 + \frac{D_{k_F}(1-\Gamma/F) - k_{F\text{ions}}\hat{S}_F/C^*\hat{D}}{1/F - D_{k_F}\ln F(1-\Gamma/F)}\ln r. \tag{17}$$

This concentration field is substituted into boundary condition (15) to obtain a nonlinear evolution equation for the coating front,

$$\frac{FF_t}{\sqrt{F^2+F_\theta^2}} = \frac{k_F}{K_F}\left[1 + \frac{D_{k_F}(1-\Gamma/F) - k_{F\text{ions}}\hat{S}_F/C^*\hat{D}}{1/F - D_{k_F}\ln F(1-\Gamma/F)}\ln F\right] \times(1-\Gamma\kappa) - \frac{k_{F\text{ions}}(\theta,t)}{K_F C^*} - \frac{\psi_s D_s \Gamma}{K_F \beta C^* \hat{S}_F^2}\frac{(\kappa_\theta/\sqrt{F^2+F_\theta^2})_\theta}{\sqrt{F^2+F_\theta^2}}, \tag{18}$$

subject to periodic boundary conditions

$$F(0) = F(2\pi), \quad F'(0) = F'(2\pi), \quad F''(0) = F''(2\pi), \quad F'''(0) = F'''(2\pi). \tag{19}$$

Equations (A10) and (A18) can equivalently be derived from (18) using the boundary perturbation expansion (16). Hence, from here forward we use (18) together with the concentration field (17) to qualitatively elucidate the stabilizing and destabilizing mechanisms for the coating growth. Quantitative discussions of these equations and mechanisms appear in Sec. VI after values for k_F and $k_{F\text{ions}}$ are developed in Secs. IV and V.

From (17) and for a fixed set of parameters, the concentration field increases in the radial direction. It follows that protruding irregularities in the coating, such as fingers and bumps, are surrounded by a higher concentration level than valleys or depressions. Also the concentration field depends highly nonlinearly on the size of F. For small values of F the concentration field is larger throughout the local region because there is less surface area on the coating to absorb the depositing atoms. This trend holds true until F becomes large enough that it is close to the source of the concentration at $r=1$. Here the decrease in concentration due to increased deposition onto the larger surface area is countered by the near proximity to the source.

The surface Damköhler number D_{k_F} also plays a key role in the features of the concentration field. For small values of D_{k_F}, due to either increased diffusion or decreased deposition rate, the concentration field approaches the constant far-field value everywhere in the local region and along the coating surface. On the other hand, for large D_{k_F} there is a greater change in concentration with position both radially into the local region and along the coating surface. These observations are shown quantitatively in Sec. VI.

One final approximation that can be made for the concentration field is to simplify (17) by replacing F with r_F, the average initial radius of the uncoated nanofiber. Under this approximation, the concentration field is not affected by perturbations in the coating surface. This type of approximation has been used for deposition onto planar surfaces.[12] This assumption is valid for all D_{k_F} for small coating thickness, and is always relevant for small D_{k_F} due to the nearly constant value of the coating profile in such highly diffusive systems. We use this approximation to simplify the numerical simulations in Sec. VI.

These qualitative observations of the concentration field provide insight into the structure of the evolution equation. Notice the first term on the right-hand side of (18), $k_F/K_F c(1-\Gamma\kappa)$, which describes the deposition of the sputtered material. Since this term is positive, it may lead to a destabilizing effect whereby bumps in the coating surface grow faster than valleys because of the increase in the concentration level. This term is composed of three contributions. The expression k_F/K_F contains deposition rate information from the MD simulations at the coating surface. Clearly c is the concentration of the deposition material at the coating surface. The expression in parentheses may be qualitatively described as $[1-\Gamma(1/\text{radius of coating})]$. Hence, smaller-radius nanofibers (or thinner coatings) result in a decrease in this term. This trend implies that a smoother coating may be achieved on smaller nanofibers even though such small nanofibers give rise to an overall larger concentration field in the local region, as discussed above. Hence, one should expect faster deposition on large-diameter nanofibers and that such fibers will have a rough coating due to enhanced growth of protruding regions. Thus, the first term of the evolution equation reveals general trends that rougher coatings develop on nanofibers with larger radii, in systems with higher levels of concentration, and in systems characterized by high rates of deposition.

The second term, $-k_{F\text{ions}}/K_F C^*$, on the right-hand side of (18) describes the etching of the coating surface due to ion bombardment. Since this term is negative, it may provide for a stabilizing or smoothing effect.

The last term on the right-hand side of (18) describes the effects of surface diffusion. This term provides a stabilizing effect. However, it is shown in Sec. VI that this effect is small except in regions of very high curvature.

IV. THE SHEATH MODEL NEAR THE HOLDER

A. Formulation

The surface reaction-rate parameters, k_F and $k_{F\text{ions}}$, are dependent upon the flux and energy of the ions in the local region. Hence, the flux and energy of the ions are needed for the MD simulations that directly determine these parameters. This section briefly describes a sheath model at the holder region to determine the flux and energy. This model relates the applied electrical potential, pressure, and temperature to the kinetic energy and flux of the ions at the coating surface. The model is nearly identical to that presented in Ref. 1. Note that any effects on the electric field due to the local bias around a nanofiber are neglected. The reason is that the nanofibers are much smaller than the thickness of the sheath at the holder. Hence, we neglect the local bias field around the individual nanofibers because these fibers are all assumed

to lie completely within the sheath at the holder. Here the larger field of the sheath dwarfs the local bias. Hence, ions travel in the y direction only rather than radially toward the center of the nanofiber. This is accounted for in the MD simulations that follow by allowing the ions to strike the coating surface through a range of incident angles.

The intent of the modeling is to connect macroscale phenomena to nanoscale phenomena by linking simple models at each length scale. Hence, in the sheath region near the holder we seek a model to reasonably approximate the physics. In the experiments we use an rf sputtering head. We are approximating the plasma as a uniform cylindrical column in an intermediate pressure regime [mean free path less than or equal to the characteristic lengths of the plasma but greater than the ratio of ion temperature to electron temperature multiplied by the characteristic length of the plasma (Lieberman and Lichtenberg[14])]. Under these cases it is reasonable to assume that the voltage drop occurs almost entirely across the sheath region.

In the experiments, which will provide a basis for comparison in Paper III of this series, a 2-in. aluminum target is sputtered in a background gas of argon. The pressure is varied between 4 and 40 mtorr, the power is varied between 50 and 150 W, and the target to substrate distance is 8 cm. No external bias is applied to the target or substrate (the substrate is grounded). We estimate, based on a uniform plasma model,[14] that the voltage difference between the target and the plasma is 500 V and the voltage difference between the substrate and the plasma is 10 V (see Fig. 1). We expect that there is a voltage field within the bulk plasma but that the variation in voltage across the bulk plasma is very small relative to the voltage change across the sheaths. Hence, we isolate the sheath models from each other even though their potential drops are linked in the sense that the voltage differences, listed above, are both due to the overall reactor applied voltage. These differences primarily distinguish the two sheath models. The sheath model at the target uses a relatively high velocity (due to the high voltage difference) local ion transport to get an approximation for the concentration of the neutral deposition material. The sheath model at the holder uses a relatively low velocity (due to the low voltage difference) ion transport to approximate the etching rate at the coating surface. Our operating conditions are near the edge of consistency with the assumptions of a uniform plasma model approximation (Lieberman and Lichtenberg[14]) and with the time-averaged model of Economou *et al.*[15] The latter is the basis for the sheath models at the target and the holder.

Similar to Ref. 1, the sheath layer at the holder, only a few millimeters in thickness, is thin relative to the size of the reactor. By ignoring the end effects, the sheath is modeled as a one-dimensional region that possesses a positive space charge due to an overabundance of positively charged ions. Temperature gradients and magnetic fields in the region are ignored. We assume the ions satisfy the continuity equation

$$\frac{d}{d\tilde{y}}(\hat{u}\hat{n}) = 0, \tag{20}$$

in which $\hat{u}(\tilde{y})$ is the velocity of the ions and $\hat{n}(\tilde{y})$ is their number density. The coordinate $\tilde{y}$ represents the distance from the holder, as shown in Fig. 1. Ions conserve momentum according to the equation

$$\hat{u}\frac{d\hat{u}}{d\tilde{y}} = -\frac{q\hat{E}}{m} + \frac{\alpha_H \hat{u}^2}{m}, \tag{21}$$

where q and m are the charge and mass associated with a single ion, and $\hat{E}$ is the local electric field. The first two terms in (21) represent inertia and electromotive force. The last term represents the effect of ions colliding with the background nonionized gas atoms or molecules, and the nanofibers. In this expression α_H represents the strength of this interaction. The magnitude of this collision term is assumed to be larger than its counterpart in Ref. 1 due to the presence of the nanofibers, which are large in comparison to the size of the nonionized gas atoms or molecules. The collision expression in (21) is a convenient physical form (proportional to velocity squared) and mathematical form (for obtaining solutions). This form replicates the expression used by Ref. 15 to simulate the frictional force on an ion as an average over all possible collisions experienced by the ion.

The gradient of the electric field is related to the charge density according to the equation

$$\frac{d}{d\tilde{y}}\hat{E} = -\frac{q\hat{n}}{\varepsilon_0}. \tag{22}$$

Here, ε_0 is the vacuum permittivity. The final field equation relates the electric field to the electrical potential:

$$\hat{E} = \frac{d\hat{V}}{d\tilde{y}}. \tag{23}$$

The Bohm criterion and quasineutrality[11,15] are used to define the boundary conditions for this system of first-order differential equations. We refer the reader to Ref. 15 for a thorough discussion of the boundary conditions. Ordinarily, this system would require four boundary conditions. However, the location $\tilde{y}=\hat{S}_H$ (see Fig. 1) at which the sheath layer ends is also an unknown and must be determined as part of the solution, so a fifth boundary condition is needed. Four boundary conditions are applied at $\tilde{y}=\hat{S}_H$,

$$\hat{n}(\hat{S}_H) = \hat{n}_p, \tag{24}$$

$$\hat{u}(\hat{S}_H) = -\sqrt{\frac{k_B T_e}{m + 2\alpha_H \lambda_D}}, \tag{25}$$

$$\hat{E}(\hat{S}_H) = \frac{k_B T_e}{2q\lambda_D}, \tag{26}$$

and

$$\hat{V}(\hat{S}_H) = \hat{V}_H, \tag{27}$$

and one at the holder surface,

$$\hat{V}(0) = 0. \tag{28}$$

In these expressions, $\hat{n}_p$ is the ion number density in the plasma, $k_B = 1.38 \times 10^{-23}$ J/K is the Boltzmann constant, T_e is the electron temperature (in Kelvin), and λ_D is the Debye length,

$$\lambda_D = \sqrt{\frac{\varepsilon_0 k_B T_e}{\hat{n}_p q^2}}. \tag{29}$$

The constant $\hat{V}_H$ that appears in (27) is the voltage. This voltage and the plasma ion density $\hat{n}_p$ are both assumed controllable and therefore specified by the operator. Therefore, all constants that appear within this system of equations are either material properties or can be experimentally controlled, at least in principle. Note that the magnitude of $\hat{V}_H$ is taken to be less than its counterpart at the target since the target is the driven electrode. Hence, the electric field will be smaller near the holder due to the smaller potential drop.

The system of equations (20)–(28) is nondimensionalized with the selection of the following scales for length, number density, velocity, electric field, and potential, respectively: λ_D, $\hat{n}_p$, $\sqrt{k_B T_e/m}$, $k_B T_e/q\lambda_D$, and $k_B T_e/q$. Dimensionless variables are hatless versions of their dimensional counterparts. The dimensionless constant

$$C_H = \frac{\alpha_H \lambda_D}{m} \tag{30}$$

arises in the nondimensionalization procedure and represents the effect of collisions in slowing the ions. The solution procedures, asymptotic for small and large values of C_H and numerical for intermediate values, for the governing equations are identical to that presented in Ref. 1 and so are not repeated here.

B. Results

The controllable operating conditions for the reactor are pressure, power, temperature, target-nanofiber distance, mat porosity, and initial nanofiber radius. These parameters and ranges of their values will be more thoroughly discussed in Part III. Representative values are used in the results that follow. Further, the voltage drop between the plasma and the holder, and the plasma density and the electron temperature depend on the applied power, the pressure, and the characteristic length scales (radius and length) of the plasma column. These dependencies will also be more thoroughly discussed in Part III of this series. Representative ranges of these values are used in the results that follow.

Dimensionless ion velocities u are plotted against distance $\tilde{y}$ from the holder in Fig. 6 for three values of the collision parameter: $C_H = 0$, 1, and 10. The assumed voltage across the sheath is $\hat{V}_H = 10$ V and the electron temperature is $T_e = 10^4$ K. The ion density $\hat{n}_p$ in the plasma (which increases with increasing power and pressure in our system) is taken as approximately 10^{15} atoms/m^3, the vacuum permittivity ε_0 of the sheath region is 8.9×10^{-12} F/m, and the charge q of the species is 1.6×10^{-19} C. The solid and dashed curves in the figure represent asymptotic and numerical results, respectively. The asymptotic and numerical results coincide for $C_H = 0$ and 10. However, the solid curve for $C_H = 1$, which is based upon the $C_H \gg 1$ asymptotic solution, does not coincide with the numerical result. We attribute the observed difference to the error in the asymptotic solution which assumes $C_H \gg 1$, a condition that is violated in this case. Similar results are obtained for electron temperatures up to $T_e = 2.6 \times 10^4$ K, which represent ranges of current interest.

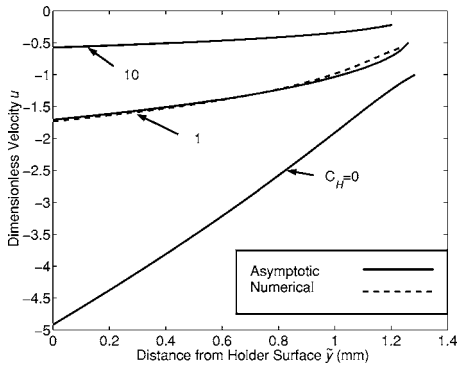

FIG. 6. Dimensionless ion velocities as a function of distance from the holder surface for several values of C_H with $\hat{V}_H = 10$ V and $T_e = 10^4$ K.

The figure also shows the sensitivity of the ion velocity to the parameter C_H: the scale of $|u|$ increases by a factor of 3 as C_H decreases from unity to zero. The sheath thickness $\hat{S}_H$ simultaneously increases modestly from approximately 1.23 to 1.28 mm. The sheath thickness corresponds to the positive distance from the holder where a curve in the figure terminates.

Figure 7 shows the kinetic energy $(m\hat{u}^2/2)$ with which ions impact the coating surface of a nanofiber at $\tilde{y} = \tilde{y}^* = 0$ (see Fig. 1; similar figures can be defined for any value of $\tilde{y}^*$ using the results for velocity shown in Fig. 6) as a function of the collision parameter C_H for two different voltages across the sheath, $\hat{V}_H = 10$ and 50 V, and two different electron temperatures, $T_e = 10^4$ and 2.6×10^4 K. Expressed as potentials $(k_B T/q)$, these electron temperatures are 0.863 and 2.24 V, respectively. The uniform plasma model suggests that the voltage across the sheath layer is on the order of 10 V under deposition conditions.[14] To see the effect of voltage on the kinetic energy, we also consider one order of magnitude more. Kinetic energies of 40 eV or more are be-

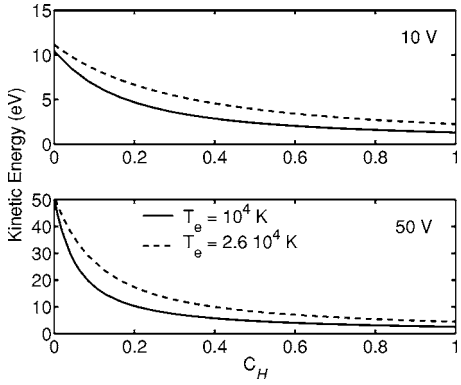

FIG. 7. Kinetic energy as a function of collision parameter.

lieved to be necessary for the material to be sputtered off the coating surface. This observation is supported by the MD simulations discussed in Sec. V.

In the top graph in Fig. 7, it is seen that the voltage $\hat{V}_H=10$ V is too low for sputtering to occur for all temperatures considered and all values of the collision parameter. The lower graph shows that when the voltage is $\hat{V}_H=50$ V, kinetic energies of 40 eV are achieved provided the collision parameter is less than about 0.05.

V. CALCULATION OF SPUTTERING AND STICKING PROBABILITIES AND RATE COEFFICIENTS BY MOLECULAR-DYNAMICS SIMULATION

Solution (17) of the local diffusion problem requires the values of two coefficients, the adsorption rate coefficient k_F and the desorption rate coefficient $k_{F\text{ions}}$, which first appeared in boundary condition (3). These coefficients are computed using a molecular-dynamics simulation at the atomic scale. The MD simulation consists of an atomic model of the system where the initial positions of the atoms or molecules and the interactions between the atoms or molecules are specified. Classical equations of motion (Newton's) are solved numerically.[7] Previously, MD calculations have been very useful for the investigation of metallic film growth by physical vapor deposition.[5,16–19] Such simulations provide the probabilities of adsorption, reflection, and sputtering events due to an incoming particle by tracking the trajectories of individual atoms.

In order to run the MD simulation, the velocity, kinetic energy and flux of the bombarding particles are specified as described in Sec. IV. The bombarding particles can be argon ions or aluminum atoms. The same simulation can be used for either particle because both have roughly the same mass and the electric charge does not appreciably affect the sputtering and adsorption processes.[3] It is assumed that the kinetic energy of an incoming argon ion is similar to that of an aluminum atom that approaches the coating surface through diffusion.

One of the unique features of the MD simulation is that the substrate surface is not flat but curved, and has a nanometer-size radius of curvature. Hence, in order to study metal coating growth on nanofibers, a model different from a flat substrate is needed. A conventional MD supercell with regular periodic boundary conditions is only useful for the simulation of the coating with small diameter and thickness. Thus, to study growth on cylindrical coatings of larger diameters similar to the experimental structures, an atomic model with modified periodic boundary conditions is created. This model consists of a slice or angular region of an Al cylindrical coating. For the atomic displacements in the azimuthal direction, angular periodicity is assumed. On the other hand, regular periodic boundary conditions are employed for the atomic displacements along the axis of the coatings. Thus, the coatings are modeled as if they are perfectly cylindrical and infinitely long. The MD simulation was run with 279 particles bombarding a curved aluminum substrate (the coating surface). The substrate consists of varying numbers of layers of Al. Varying the number of layers allows us to vary the thickness of the coating. This observation is important for the curve-fitting procedure to determine k_F and $k_{F\text{ions}}$. Further, due to the number of atoms involved, it is not possible to simulate the entire coating surface with a single MD simulation. Hence, only a sector of the surface is considered and the angular (θ) variations of k_F and $k_{F\text{ions}}$ are determined from the angle of incidence data.

The above discussion only concerns growth onto an existing coating surface. The overall growth of the coatings on polymer nanofibers is hundreds of angstroms in thickness. The growth on the polymer surface of the nanofiber represents only the initial stage of the growth process. We have chosen to simulate the main growth that occurs after the polymer surface is covered by aluminum. Thus we assume there is already a layer of Al on the surface of the nanofiber. For the next body of work we are investigating the initial stages of coating by considering models for nucleation sites on the polymer surface.

The interaction between the aluminum atoms is modeled by an extensively tested embedded-atom-type (or glue-type) potential[20] with a repulsive potential[17] for the short-range interaction of Al atoms with kinetic energies above 10 eV. Molecular-dynamics simulations are performed and structures are relaxed at different constant reactor temperatures ranging from 300 to 500 K using the velocity scaling algorithm. The initial simulation cell includes a 30° angular portion of the coating with 34-nm inner diameter, 2.0-nm length in the axial direction, and a 2.0-nm coating thickness that contains 2811 atoms. As the coating thickness increases, only the outermost 2.0 nm of the coating is included in the simulation cell. The initial structure is created from a fcc Al crystal structure with the (111) surface facing radially outwards. This surface structure is selected because it has the lowest formation energy and it has been used in other MD simulations of thin-film growth on flat surfaces.[17] Thus we can compare our results with other investigations. We believe the MD results do not strongly depend on the selection of this surface structure because the temperature is high (500 K) and the overall geometry of the surface (flat or curved) is found to be more important. If the temperature were low, then the surface structure would be important as there would be particular peaks in the adsorption and reflection probability graphs related to the surface structure.

In the boundary regions, atom pairs are investigated and if the distance between the atoms is less then 2 Å, one of the atoms is removed. The positions of the innermost atoms that are within a radial distance of 34.5 nm from the coating axis are fixed and all the other atoms are relaxed. After relaxing the coating's atomic structure at constant temperatures of 300 and 500 K, we found that the coating preserved its shape and only the atoms in or close to the boundary regions had additional displacements.

Estimating the standard error[7] we found that it is around 4% for the flat surface simulations and 4%–6% for the coating simulations. This error estimate is comparable with other MD simulations that used 200 impinging Al atoms and reported less than 5% error.[17] Considering these error estimates

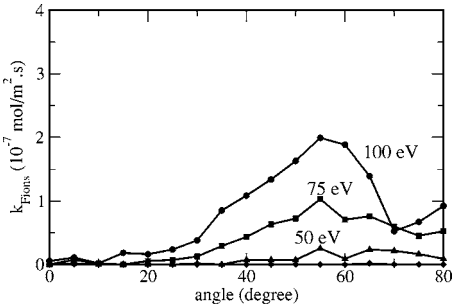

FIG. 8. Values of k_{Fions} as a function of incident angle for incoming argon ions with kinetic energies of 25, 50, 75, and 100 eV, and for a coating thickness of 2.0 nm.

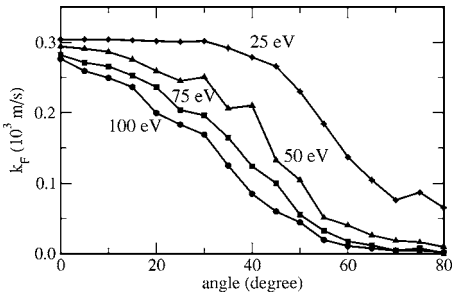

FIG. 9. Values of k_F as a function of incident angle for incoming aluminum atoms with kinetic energies of 25, 50, 75, and 100 eV, and for a coating thickness of 2.0 nm.

we believe 279 impinging atoms per energy per angle are sufficient. This number of atoms is above the numbers used in other MD simulations.[17,21]

The next step in MD simulations of metal coating growth is the calculation of the rate coefficients, k_F and k_{Fions}, by bombarding the coating surface with argon ions or aluminum atoms. The kinetic energies of the incoming argon ions are specified to be 25, 50, 75, and 100 eV. These values are in the range suggested by the sheath model. Incident angles of 0°–80° from the normal to the coating surface with a 5° increment were used in order to determine the angular dependence of k_F and k_{Fions}. Since the geometry of the coating surface is cylindrical, the surface is not symmetrical with respect to the bombarding ions as is a flat surface. Thus, the lateral component of the initial velocity of the impinging particles is selected either parallel or perpendicular to the axis of the cylindrical coating. A single run (279 particles at one kinetic energy at one incident angle) takes about 24 h to complete on an INTEL-based workstation.

In order to obtain the desorption rate k_{Fions} for a fixed incident angle, the 279 bombarding particles are sent in one at a time and the number of aluminum atoms sputtered off the surface is counted. The ratio of this number to 279 (the number of incoming argon ions) is computed. This ratio is multiplied by the flux $\hat{n}\cdot\hat{u}$ from the holder sheath model and divided by Avogadro's number to get k_{Fions} at a particular coating thickness. The experiment is repeated with different incident angles to obtain the angular dependence of k_{Fions}.

Figure 8 shows the values of k_{Fions} as a function of incident angle for incoming argon ions with kinetic energies of 25, 50, 75, and 100 eV, which are consistent with the sheath model. As expected, k_{Fions} increases with kinetic energy. Further, k_{Fions} tends to achieve a maximum value for incident angles around 55°. The k_{Fions} value stays relatively high at the very large grazing angles of 75°–80°. We believe this is due to the cylindrical geometry since it is easier to etch the atoms away from the coating surface by particles bombarding the surface in the direction perpendicular to the axis of the coating.

In order to obtain the adsorption rate k_F for a fixed incident angle, the incoming particles are now considered to be aluminum atoms that hit the substrate via diffusion. The 279 bombarding particles are sent in one at a time and the number of aluminum atoms that are adsorbed is counted. The ratio of this number to 279 (the number of incoming aluminum atoms) is computed. This ratio is multiplied by the velocity of the aluminum atoms to determine k_F at a particular coating thickness. This velocity is estimated using the expression $\sqrt{k_BT/m_{Al}}$ where m_{Al} is the mass of an aluminum atom. For this calculation it is also assumed that the sputtered atoms eventually equilibrate at $T=300$ K.

Figure 9 shows the values of k_F as a function of incident angle for incoming aluminum atoms with kinetic energies of 25, 50, 75, and 100 eV. It is seen that k_F decreases with kinetic energy, since highly energetic atoms do not easily adsorb onto the coating surface. Further, atoms that strike the surface with normal incidence are more likely to adsorb. Additionally, atoms that strike the surface with incidence nearly parallel to the surface (incident angle near 90°) do not easily attach to the surface. This is in contrast to the results for the flat surface obtained in Ref. 1. There, atoms that grazed the surface tended to stick. We attribute the attachment difference to the high degree of curvature of the coating.

Figure 10 shows the values of k_F and k_{Fions} as a function of the kinetic energy of the incoming particles for normal incidence, consistent with the radially dominant diffusion transport model. We see from Figs. 9 and 10 that k_F is nearly constant for normal incidence, as mentioned for (A2). Hence, we take it to be a constant in the level set simulations that follow. Also k_{Fions} increases with kinetic energy and, as

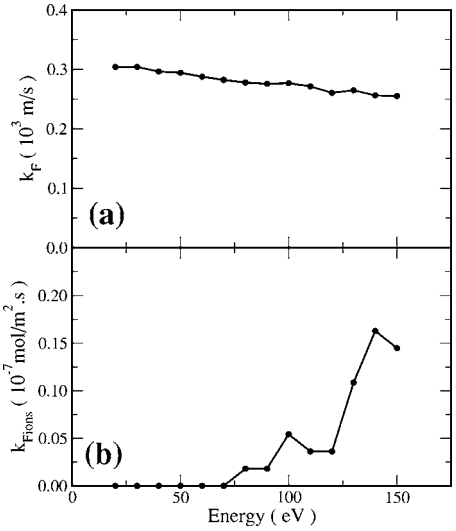

FIG. 10. Values of k_F and k_{Fions} as a function of the kinetic energy of the incoming particles for normal incidence.

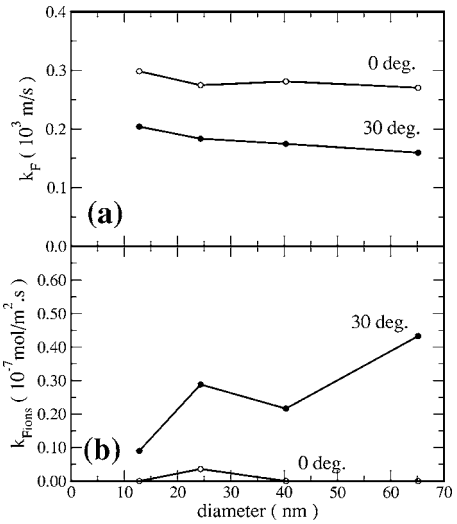

FIG. 11. $k_{F\text{ions}}$ and k_F for a fixed kinetic energy of the incoming particles and a fixed incident angle as a function of coating thickness.

stated earlier, kinetic energies of 40 eV and higher are needed to achieve sputtering of material from the curved coating.

Figure 11 shows the values of $k_{F\text{ions}}$ and k_F for a fixed kinetic energy of the incoming particles and a fixed incident angle θ as a function of coating thickness. This figure further supports our decision to keep k_F constant. Additionally, we see that $k_{F\text{ions}}$ is smallest for small curvature. Thus it is harder to sputter atoms from surfaces with very small radius than from flat surfaces.

VI. LEVEL SET SIMULATIONS OF THE COATING SURFACE

The analytical models of Sec. III provide insight into the mechanisms involved in coating growth. In this section, we employ a numerical model based upon the level set method[22] to simulate growth of the coating front. This numerical method, which is described below, is used to conduct a parametric study to further our understanding of the mechanisms of coating growth.

In the level set method, the front $r=F(\theta,t)$ is represented as the zero isocontour of the level set function $\phi(r,\theta,t)$, which satisfies the evolution equation

$$\phi_t + \hat{v}_n |\nabla \phi| = 0, \tag{31}$$

where $\hat{v}_n$ is the normal velocity (4). As is typical of level set problems, the only difficulty in the implementation is in the computation of the normal velocity. There are two features of the normal velocity that complicate the computation: (i) the second derivative of curvature with respect to arclength is needed, and (ii) the concentration of aluminum atoms at the front is needed.

The curvature derivative is handled by requiring that the front location $r=F(\theta,t)$ remain a single-valued polar function. The advantage of this assumption is that the numerical derivatives are simple to compute.[23] On the other hand, the restriction is undesirable because it prohibits the front from forming mushroom-shaped tendrils. However, many of the experimental runs show single-valued cross sections, so the assumption is valid over a wide range of typical operating conditions for the system.

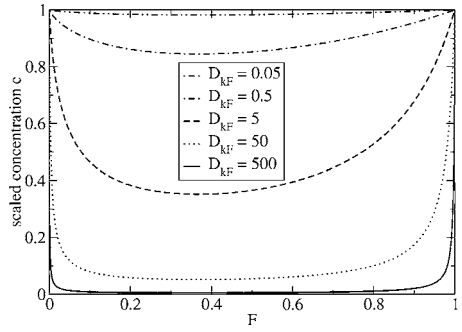

FIG. 12. Concentration at the front as a function of nondimensional coating radius F.

For simplicity the approximate concentration (17) is used. This approach is similar to that in Ref. 12. Further, we follow Ref. 12 by replacing F with r_F, the average initial radius of the uncoated nanofiber, in (17).

The main issue in coating morphology is the interplay among the mechanisms of deposition, etching, and surface diffusion as embodied in the three respective terms on the right-hand side of the evolution equation (18). Due to the considerable uncertainty associated with the values of several material constants that appear in the model, a parametric study is conducted. Preliminary analysis suggests values for several parameters that are held constant in the study:

$k_{F\text{ions}}$: 0.0 mole/m^2 s,
β: 9.6×10^{21} nm^3/mole,
$\hat{S}_F$: 500 nm,
$\hat{D}$: 7.5×10^{13} nm^2/s.

Observe that we have set $k_{F\text{ions}}$, the parameter that controls the rate of etching (or desorption), to zero based upon the low values for this parameter obtained through the MD simulations. More correctly we are ignoring the desorption term $E_C=k_{F\text{ions}}/K_F C^*$ in (18). Data from Fig. 10 together with values for C^* listed below indicate that the size of this term is on the order of 10^{-2}, whereas the size of the deposition term is order one. Therefore, with the exception of Fig. 23, only the mechanisms of deposition and surface diffusion play a role in the following parametric study. The parameters that are varied (with indicated ranges) include the concentration of neutral species $C^*(6\times10^{-37}$ to 6×10^{-36} moles/nm^3), the reaction rate coefficient at the fiber $k_F(7.5\times10^{11}$ to 7.5×10^{13} nm/s), the surface diffusion component $\psi_s D_s(6.5$ to 1.5×10^2 nm^3/s), and the capillary length scale $\hat{\Gamma}(0.0101$ to 0.2020 nm). Note that k_F and C^* are calculated by the model, β is the molar volume for aluminum, and $\hat{D}$, $\hat{\Gamma}$, and $\psi_s D_s$ are estimated from the literature.[12]

Concentration at the front. The concentration at the front is approximated by (17) evaluated at $r=F$. Figure 12 shows how this concentration depends on the radius of the coating (recall that $r=1$ is half the distance between fibers). As discussed in Sec. III, the concentration field varies highly non-

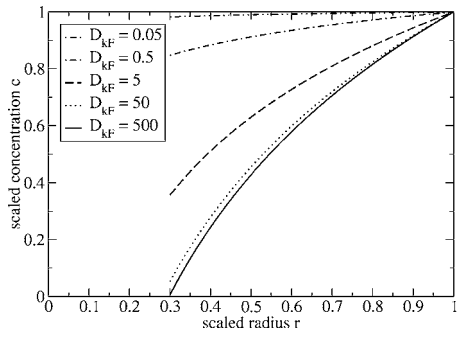

FIG. 13. Concentration off the front as a function of radius, for an initial nondimensional nanofiber radius of 0.3.

linearly with the size of F. For small values of F the concentration field is larger throughout the local region because there is less surface area on the coating to absorb the depositing atoms. This trend holds true until F becomes large enough that it is close to the source of the concentration at $r=1$. Here the increased loss of concentration due to increased deposition onto the larger surface area is countered by the near proximity to the source.

From (17) and for a fixed set of parameters, the concentration field increases with radius, as shown in Fig. 13. It follows that protruding irregularities in the coating, such as fingers and bumps, are surrounded by a higher concentration level than valleys or depressions. Hence, bumps see a higher concentration than valleys, leading to a higher rate of deposition on the bumps. Further, the surface Damköhler number D_{k_F} plays a key role in the features of the concentration field. For small values of D_{k_F}, due to either increased diffusion or a decrease in the deposition, Figs. 12 and 13 show that the concentration field approaches the constant far-field value everywhere in the local region and along the coating surface. On the other hand, for large D_{k_F} there is a greater change in concentration with position both radially into the local region and along the coating surface. Hence, when D_{k_F} is large, the deposition dominates and bumps will grow, leading to a rough surface. When D_{k_F} is small, diffusion dominates and dips will fill in faster, leading to a smoother surface. These predictions are verified in the simulations of the coating surface that follow.

Standard parameter set. Our experiments show that in 15 min, the coating grows about 20–30 nm. Simulations using three different initial fiber profiles were run to calibrate the model. The parameter set

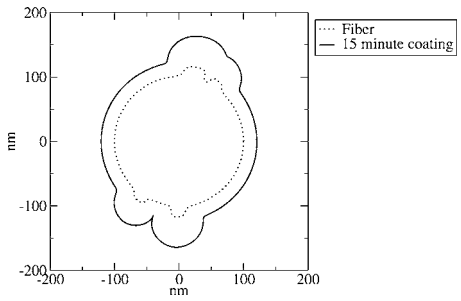

FIG. 14. Coating growth using the standard parameter set with large bumps.

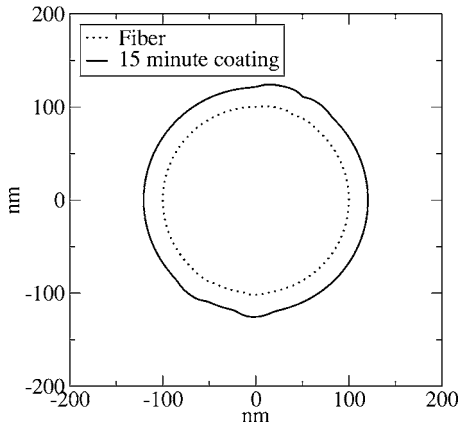

FIG. 15. Coating growth using the standard parameter set with small bumps.

k_F: 7.5×10^{12} nm/s,
C^*: 3×10^{-36} mole/nm^3,
$\hat{\Gamma}$: 0.0505 nm,
$\psi_s D_s$: 6.5 nm^3/s,
D_{kF}: 50

was determined to yield results that match the experimental results. The three profiles are shown in Figs. 14–16. The fiber shown in Fig. 14 has a circular cross section with four bumps that have magnitudes of 20% and 14% of the fiber radius. The fiber shown in Fig. 15 has a circular cross section with four bumps that have magnitudes of 2% and 1.4% of the fiber radius. The fiber shown in Fig. 16 has a circular cross section with several Fourier modes superposed atop it. These modes are consistent with models of the landscape of electrospun nanofibers.[8,9] In each case, the coating growth after 15 min is about 20–30 nm in the smoother regions. There is faster growth at the bumps; this phenomenon is described below.

Varying the concentration. The concentration of aluminum atoms in the plasma surrounding the fiber plays a significant role in the coating process. The value of the concentration increases as the system power and pressure are increased. Figure 17 shows the effect of varying the concentration over one order of magnitude. Here, the standard parameter set is used for the other parameters. Clearly there is

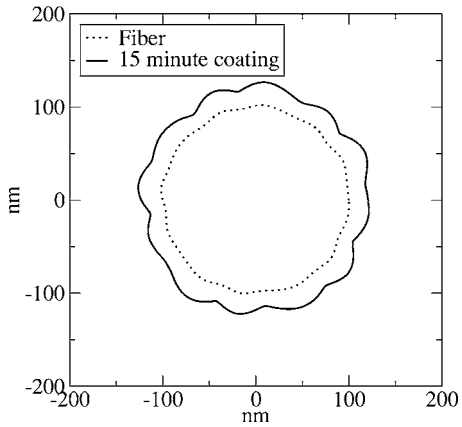

FIG. 16. Coating growth using the standard parameter set with Fourier modes.

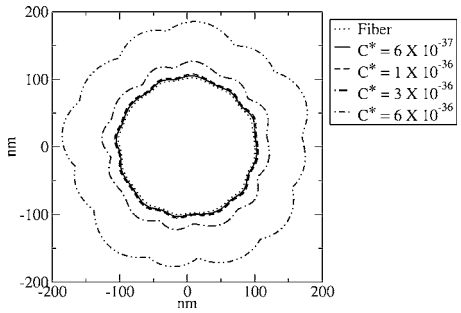

FIG. 17. The effect of changing concentration with $D_{k_F}=50$.

a significant increase in growth as C^* increases.

Varying the Damköhler number D_{k_F}. The Damköhler number D_{k_F} is the ratio of the rate of deposition of aluminum on the fiber to the rate of transport of aluminum to the fiber via diffusion. Hence, as D_{k_F} increases, the expectation is that the coating growth accelerates, because the model assumes an unlimited supply of aluminum atoms at the outer computational boundary. Also, because of the sharp increase in concentration as radius increases (Fig. 13), bumps in the coating surface should grow faster, leading to a rougher surface. Figure 18 shows that this is indeed the case. With $D_{k_F}=5$, diffusion dominates and the surface is smoothed. When D_{k_F} is raised to 50, there is little change, but when D_{k_F} is set to 500, the roughening effect is clearly visible. Here, the concentration $C^*=1\times10^{-36}$ was used.

Varying the bump size. Given the sharp increase in concentration as the radius increases (Fig. 13), larger bumps should grow faster than smaller bumps, all else being equal. This effect is clearly shown in Figs. 19 and 20. As a convenient reference point, consider the growth along the ray $\theta=3\pi/2$, at the bottom bump. The small bump in Fig. 19 grows about 5.4 nm in 15 min, while the large bump in Fig. 20 grows about 11.5 nm in 15 min. It is interesting to note that the growth of tiny bumps is exaggerated when the Damköhler number is sufficiently high because experimental results indicate that the coating surface often roughens, and a high Damköhler number provides a possible explanation for the underlying physical mechanism. In these figures, $D_{k_F}=50$ and $C^*=1\times10^{-36}$.

Varying the surface diffusion. The expectation is that a change in the surface diffusivity component $\psi_s D_s$ causes a change in the smoothness of the coating without changing the overall growth rate. The simulation was run using the

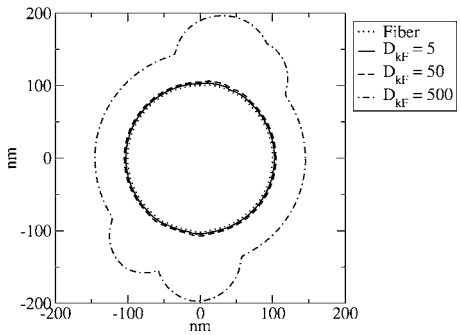

FIG. 18. The effect of changing D_{k_F} with concentration $C^*=1\times10^{-36}$.

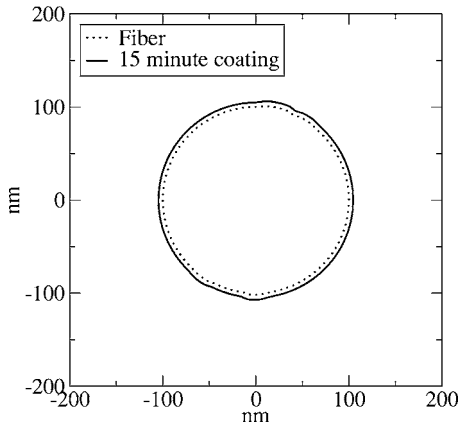

FIG. 19. The growth of small bumps when $D_{k_F}=50$ and $C^*=1\times10^{-36}$.

standard parameter set, with $\psi_s D_s$ ranging from 6.5 to 1.5×10^2. Figure 21 shows the coating growth for this range of values. For smaller values of $\psi_s D_s$, the coating is virtually indistinguishable from that with $\psi_s D_s=6.5$. As expected, the surface is noticeably smoother when more surface diffusion occurs, as shown in Fig. 22, which zooms in on the cusp region at the bottom of Fig. 21.

Varying the capillary length. When the value of $\hat{\Gamma}$ is varied from 0.0101 to 0.2020, there is essentially no difference in the coating growth after 15 min.

Varying the etching number E_C. The effects of etching of the coating surface due to ion bombardment were neglected in the previous simulations due to the size of E_C (10^{-2}). Figure 23 displays a parametric study of the influence of increasing E_C. Clearly there is less growth as E_C increases. However, this effect is not significant until E_C is much larger than 10^{-2}, in which case the growth is noticeably slowed.

VII. SUMMARY

The coating of nanoscale structures and the evolution of crystalline structures at the nanoscale are and will continue to be important issues. We develop a comprehensive model integrating across atomic to continuum length scales for simulating the sputtering, transport, and deposition of a coating material onto a nanoscale substrate. The intent of the comprehensive model is to connect macroscale phenomena

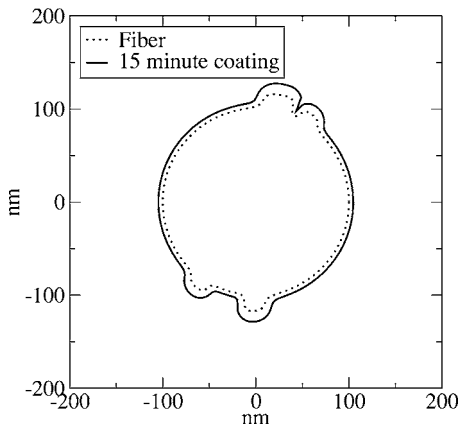

FIG. 20. The growth of large bumps when $D_{k_F}=50$ and $C^*=1\times10^{-36}$.

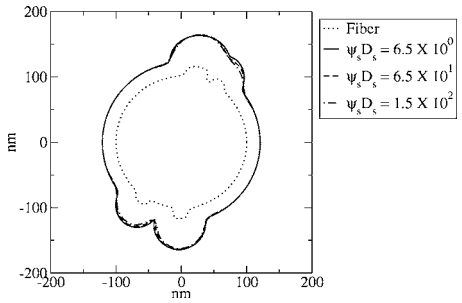

FIG. 21. The effect of the surface diffusion component ($\psi_s D_s$) for the standard parameter set.

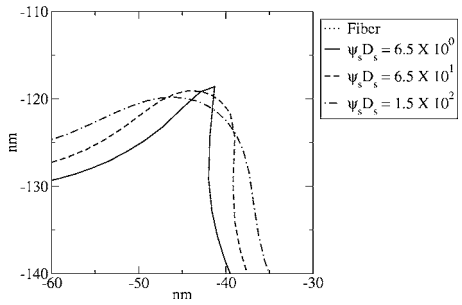

FIG. 22. Local view of the coating surface of the region near the bottom of Fig. 21.

to nanoscale phenomena by linking simple models at each length scale. The solution procedure is critical to this intent. Hence, we have made many simplifying assumptions to piece together a collection of simple submodels into one comprehensive model. We plan to revisit each submodel in future efforts to improve the comprehensive model.

In this paper the interrelationships among processing factors for the sputtering, transport, and deposition are investigated from a detailed modeling approach that describes the salient physical and chemical phenomena. Solution strategies that couple continuum and atomistic models are used. Information is passed between the various length scale models so that the simulations are integrated together. To keep the numerical simulations at a manageable level, asymptotic analyses are used to reduce the complex models to simpler, but still relevant, models.

In Part I of this series, we described a model of the sheath region at the target and the reactor dynamics near the target surface.[1] The reactor model determined the concentration of the coating material.

In Part II of this series (this paper) we describe the sheath region at the holder and the local dynamics near the substrate surface. The concentration from Part I is used as input to this local model. At the atomic level, we use molecular dynamics (MD) simulations to study the sputtering and deposition mechanisms at a curved surface. Ion kinetic energies and fluxes are passed from the continuum sheath model to these MD simulations. These simulations calculate sputtering and sticking probabilities that in turn are used to calculate parameters for the local model. The local model determines an evolution equation for the coating surface. Parametric studies of this equation reveal general trends that rougher coatings develop on nanofibers with larger radii, in systems with higher levels of concentration, and in systems characterized by high rates of deposition.

The model we have developed provides reasonable trends with respect to the coating evolution on nanoscale structures and how that evolution depends on process parameters. To become more useful to the application engineer, we must now benchmark the model against experimental data as the processing parameters are varied. This benchmarking is the subject of Part III of this series. With a validated model we can then predict how coating properties will change with deposition conditions for similar geometries. This predictive capability will be quite useful as the size of solid-state optoelectronic components continues to decrease.

ACKNOWLEDGMENTS

This work was supported by NSF Grant Nos. DMS 03-05580 and DMI-0403835, and NASA Grant Nos. NCC3-1094 and NNC04GB27G.

APPENDIX: SOLUTION BY BOUNDARY PERTURBATION

As discussed in Sec. III B we make three assumptions to make analytical progress in the solution of (10)–(12) and (15): (i) the rate of growth of the front compared to the rate of diffusional transport is negligible ($Q_F \ll 1$, so the system is quasistatic), (ii) the coating is nearly circular, and (iii) derivatives of the concentration and of the two rate constants with respect to θ are negligible at leading order. The second assumption corresponds to the perturbation expansion (16). The third assumption is equivalent to the three fields c, k_F, and $k_{F\text{ions}}$ possessing the following perturbation expansions:

$$c = c_0(r) + Ac_1(r,\theta) + \cdots, \tag{A1}$$

$$k_F = k_{F_0} + Ak_{F_1}(\theta) + \cdots, \tag{A2}$$

$$k_{F\text{ions}} = k_{F\text{ions}_0} + Ak_{F\text{ions}_1}(\theta) + \cdots. \tag{A3}$$

The latter two expressions account for θ-dependent adsorption and etching at the coating front. In the above, the leading-order terms are independent of θ, but may depend upon $f(t)$. This point is elaborated upon further in the description of how MD simulations are used to obtain k_F and $k_{F\text{ions}}$. Those simulations predict that for aluminum and the operating conditions of our reactor, k_{F_0} is a constant (K_F) and k_{F_1} is negligibly small. Nevertheless, we assume the form (A2) for generality. Also due to this expansion for k_F, D_{k_F} is expanded similarly ($D_{k_{F_0}}$ is the leading-order term).

The leading-order concentration problem is

$$0 = c_{0_{rr}} + \frac{1}{r}c_{0_r} \tag{A4}$$

together with boundary conditions

$$c_0 = 1 \quad \text{on } r = 1, \tag{A5}$$

$$c_{0_r} = D_{k_{F_0}} c_0 \left(1 - \frac{\Gamma}{f}\right) - J_0 \quad \text{on } r = f, \tag{A6}$$

and

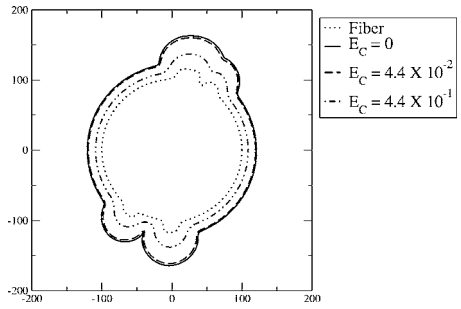

FIG. 23. Coating growth using the standard parameter set and nonzero E_C.

$$f_t = c_0\left(1-\frac{\Gamma}{f}\right) - \frac{k_{F\mathrm{ions}_0}}{K_F C^*} \quad \text{on } r=f, \tag{A7}$$

where $J_0 = k_{F\mathrm{ions}_0}\hat{S}_F/C^*\hat{D}$. In (A7) $\partial^2\kappa/\partial s^2 = 0$ due to the angular independence of $f(t)$. Further, the MD simulations predict that for aluminum and the operating conditions of our reactor, the etching terms $k_{F\mathrm{ions}_0}/K_F C^*$ and J_0 are small compared to the deposition term. Hence, we neglect the etching terms.

The general solution to (A4) is $c_0 = a(t)\ln r + b(t)$. Applying boundary conditions (A5) and (A6), it is seen that $b(t) = 1$ and

$$a(t) = \frac{D_{k_{F_0}}(f-\Gamma)}{1 - D_{k_{F_0}}\ln f(f-\Gamma)}. \tag{A8}$$

So the leading-order concentration is

$$c_0 = 1 + \left[\frac{D_{k_{F_0}}(f-\Gamma)}{1 - D_{k_{F_0}}\ln f(f-\Gamma)}\right]\ln r. \tag{A9}$$

Substituting the leading-order concentration into boundary condition (A7), we develop a nonlinear ordinary differential equation describing the free boundary of the circular coating shape:

$$f_t = \left\{\left[\frac{D_{k_{F_0}}(f-\Gamma)}{1 - D_{k_{F_0}}(f-\Gamma)\ln f}\right]\ln f + 1\right\}\left(1-\frac{\Gamma}{f}\right). \tag{A10}$$

The solution of (A10) defines the leading-order radius f of the coating at time t and is shown in Fig. 24. This solution gives an estimate of the time to achieve a desired coating thickness. This solution is also needed to complete the description of the leading-order concentration field through (A9).

The leading-order problem, however, can only give insight into the growth of radially uniform coatings. To understand how a coating can grow nonuniformly, we must consider the order A problem for both c_1 and $g(\theta,t)$.

The order A concentration problem is

$$c_{1_{rr}} + \frac{1}{r}c_{1_r} + \frac{1}{r^2}c_{1_{\theta\theta}} = 0 \tag{A11}$$

together with the boundary conditions

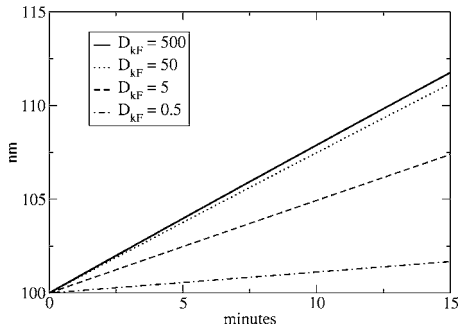

FIG. 24. Dimensional plot of the radius of the circular coating shape as a function of time ($\hat{\Gamma}=0.0505$ nm, $\hat{S}_F=500$ nm, $J_0=0$, and $\hat{f}(0)=100$ nm).

$$c_1 = 0 \quad \text{on } r=1, \tag{A12}$$

and

$$c_{0_{rr}}g + c_{1_r} = D_{k_{F_1}}(\theta)c_0\left(1-\frac{\Gamma}{f}\right) + D_{k_{F_0}}(c_{0_r}g + c_1)\left(1-\frac{\Gamma}{f}\right) + D_{k_{F_0}}c_0\Gamma\left(\frac{g}{f^2}+\frac{g_{\theta\theta}}{f^2}\right) - J_1(\theta) \quad \text{on } r=f, \tag{A13}$$

where $J_1(\theta) = k_{F\mathrm{ions}_1}\hat{S}_F/C^*\hat{D}$.

While it is possible to solve this problem using eigenfunction expansions, we shall instead for simplicity assume that $c_{1_{\theta\theta}} \ll 1$. Hence, (A11) has as general solution

$$c_1 = a_1(\theta,t)\ln r + b_1(\theta,t), \tag{A14}$$

where $a_1(\theta,t)$ and $b_1(\theta,t)$ are functions of integration. Applying boundary condition (A12), we find that

$$b_1 = 0. \tag{A15}$$

After substituting (A14) into boundary condition (A13), we determine

$$-\frac{a}{f^2}g + \frac{a_1}{f} = D_{k_{F_1}}(1+a\ln f)\left(1-\frac{\Gamma}{f}\right) + D_{k_{F_0}}\left(\frac{a}{f}g + a_1\ln f\right) + D_{k_{F_0}}(1+a\ln f) \times \Gamma\left(\frac{g}{f^2}+\frac{g_{\theta\theta}}{f^2}\right) - J_1(\theta). \tag{A16}$$

From here a_1 is found to be

$$a_1 = \frac{[(a/f^2)g]f}{1 - D_{k_{F_0}}\ln f(f-\Gamma)} + \frac{[D_{k_{F_1}}(1+a\ln f)(1-\Gamma/f)]f}{1 - D_{k_{F_0}}\ln f(f-\Gamma)} + D_{k_{F_0}}\frac{[(a/f)g]}{1 - D_{k_{F_0}}\ln f(f-\Gamma)}f + D_{k_{F_0}}\frac{D_{k_{F_0}}(1+a\ln f)\Gamma(g/f^2 + g_{\theta\theta}/f^2)}{1 - D_{k_{F_0}}\ln f(f-\Gamma)}f - \frac{J_1(\theta)f}{1 - D_{k_{F_0}}\ln f(f-\Gamma)}. \tag{A17}$$

Using c_1 evaluated at $r=f$ and the order A expansion of (15), we determine a differential equation describing the front perturbation $g(\theta,t)$,

$$g_t = c_{0_r}(r=f)g\left(1-\frac{\Gamma}{f}\right)+c_1(r=f)\left(1-\frac{\Gamma}{f}\right)+c_0(r=f) \times\Gamma\left(\frac{g}{f^2}+\frac{g_{\theta\theta}}{f^2}\right)-\left(\frac{k_{F\mathrm{ions}}}{K_F C^*}\right)_1+\frac{\psi_s D_s \Gamma}{K_F \beta C^* \hat{S}_F^2}\frac{(g_{\theta\theta}+g_{\theta\theta\theta\theta})}{f^4}. \tag{A18}$$

The structure of this equation provides insight into the mechanisms defining the morphology of the coating front as discussed in Sec. III B. Further, we use the boundary perturbation structure (16) as input to an analysis describing the response of the coated nanostructures to applied electric fields.[24] Hence, our approach links models across the entire fabrication process with models for the application of the coated nanostructures.

[1] A. Buldum *et al.*, preceding paper, J. Appl. Phys. **98**, 044303 (2005).
[2] W. Liu, M. Graham, E. A. Evans, and D. H. Reneker, J. Mater. Res. **17**, 3206 (2002).
[3] U. Hansen, S. Rodgers, and K. Jensen, Phys. Rev. B **62**, 2869 (2000).
[4] V. Sukharev, Vacuum **65**, 281 (2002).
[5] P. Vogel, U. Hansen, and V. Fiorentini, Comput. Mater. Sci. **24**, 58 (2002).
[6] H. Wadley, X. Zhou, R. Johnson, and M. Neurock, Prog. Mater. Sci. **46**, 329 (2001).
[7] M. P. Allen and D. J. Tildesley, *Computer Simulation of Liquids* (Oxford University Press, Oxford, 1996).
[8] A. L. Yarin, S. Koombhongse, and D. H. Reneker, J. Appl. Phys. **90**, 4836 (2001).
[9] A. L. Yarin, S. Koombhongse, and D. H. Reneker, J. Appl. Phys. **89**, 3018 (2001).
[10] D. J. Economou and R. C. Alkire, J. Electrochem. Soc. **135**, 2786 (1988).
[11] M. Gegick and G. W. Young, SIAM J. Appl. Math. **54**, 877 (1994).
[12] J. Thiart and V. Hlavacek, AIChE J. **41**, 1926 (1995).
[13] O. A. Louchev and Y. Sato, J. Appl. Phys. **84**, 6673 (1998).
[14] M. A. Lieberman and A. J. Lichtenberg, *Principles of Plasma Discharges and Materials Processing* (Wiley, New York, 1994).
[15] D. J. Economou, D. R. Evans, and R. C. Alkire, J. Electrochem. Soc. **135**, 756 (1988).
[16] A. Zhou and H. N. G. Wadley, Surf. Sci. **431**, 42 (1999).
[17] U. Hansen, P. Vogl, and V. Fiorentini, Phys. Rev. B **59**, R7856 (1999).
[18] D. E. Hanson, A. F. Voter, and J. D. Kress, J. Appl. Phys. **82**, 3552 (1997).
[19] D. G. Coronell, D. E. Hanson, A. F. Voter, C. L. Liu, and J. D. Kress, Appl. Phys. Lett. **73**, 3860 (1998).
[20] F. Ercolessi and J. B. Adams, Europhys. Lett. **26**, 583 (1994).
[21] A. Kersch and U. Hansen, J. Vac. Sci. Technol. A **20**, 1284 (2002).
[22] S. Osher and R. Fedkiw, *Level Set Methods and Dynamic Implicit Surfaces* (Springer, New York, 2003).
[23] X. Zheng, Master thesis, University of Akron, 2003.
[24] T. Marinov, A. Buldum, C. B. Clemons, K. L. Kreider, G. W. Young, and S. I. Hariharan, J. Appl. Phys. (to be published).